Titanates of the lindsleyite–mathiasite (LIMA) group reveal isotope disequilibrium associated with metasomatism in the mantle beneath Kimberley (South Africa)

Giuliani, Andrea; Woodhead, Jon D.; Phillips, David; Maas, Roland; Davies, Gareth R.; Griffin, William L.

published in
Earth and Planetary Science Letters
2018

DOI (link to publisher)
10.1016/j.epsl.2017.11.014

document version
Publisher's PDF, also known as Version of record

Earth and Planetary Science Letters 482 (2018) 253–264

Contents lists available at ScienceDirect

Earth and Planetary Science Letters

www.elsevier.com/locate/epsl

Titanates of the lindsleyite–mathiasite (LIMA) group reveal isotope disequilibrium associated with metasomatism in the mantle beneath Kimberley (South Africa)

Andrea Giuliani [a,b,c,*], Jon D. Woodhead [d], David Phillips [a], Roland Maas [d], Gareth R. Davies [c], William L. Griffin [b]

[a] KiDs (Kimberlites and Diamonds), School of Earth Sciences, The University of Melbourne, Parkville, 3010 Victoria, Australia
[b] ARC Centre of Excellence for Core to Crust Fluid Systems and GEMOC, Department of Earth and Planetary Sciences, Macquarie University, North Ryde, 2109 NSW, Australia
[c] Department of Earth Sciences, VU Amsterdam, De Boelelaan 1085, 1081 HV Amsterdam, The Netherlands
[d] Melbourne Isotope Geochemistry, School of Earth Sciences, The University of Melbourne, Parkville, 3010 Victoria, Australia

ARTICLE INFO

Article history:
Received 2 August 2017
Received in revised form 21 October 2017
Accepted 7 November 2017
Available online 23 November 2017
Editor: F. Moynier

Keywords:
LIMA
mantle xenoliths
Sr isotope disequilibrium
metasomatism
Kimberley

ABSTRACT

Radiogenic isotope variations unrelated to radiogenic ingrowth are common between minerals found in metasomatised mantle xenoliths entrained in kimberlite, basalts and related magmas. As the metasomatic minerals are assumed to have been in isotopic equilibrium originally, such variations are typically attributed to contamination by the magma host and/or interaction with mantle fluids during or before xenolith transport to surface. However, the increasing evidence of metasomatism by multiple, compositionally distinct fluids permeating the lithospheric mantle, coeval with specific magmatic events, suggests that isotopic disequilibrium might be a consequence of discrete, though complex, metasomatic events.

Here we provide clear evidence of elemental and Sr isotope heterogeneity between coeval Ti-rich LIMA (lindsleyite–mathiasite) minerals at the time of their formation in the mantle. LIMA minerals occur in close textural association with clinopyroxene and phlogopite in low-temperature (~800–900 °C), strongly metasomatised mantle xenoliths from the ~84 Ma Bultfontein kimberlite (South Africa). Previous U/Pb dating of the LIMA phases was used to argue that each xenolith recorded a single event of LIMA crystallisation at ~180–190 Ma, coeval with the emplacement of Karoo magmas. SEM imaging reveals that up to four types of LIMA phases coexist in each xenolith, and occasionally in a single LIMA grain. Major element and *in situ* Sr isotope analyses of the different LIMA types show that each phase has a distinct elemental composition and initial $^{87}Sr/^{86}Sr$ ratio (e.g., 0.7068–0.7086 and 0.7115–0.7129 for two LIMA types in a single xenolith; 0.7053-0.7131 across the entire sample suite).

These combined age and isotopic constraints require that multiple fluids metasomatised these rocks at broadly the same time (i.e. within a few thousands to millions of years), and produced similar mineralogical features. Elemental and isotopic variations between different LIMA types could be due to interaction between one (or more) Karoo-related Ti-rich silicate melts and previously metasomatised, phlogopite-rich lithospheric mantle. This study demonstrates that mantle metasomatic assemblages seemingly generated in a single event may instead result from the infiltration of broadly coeval fluids with variable compositions. This in turn implies that the isotopic variations recorded in mantle rocks may be an inherent feature of metasomatism, and that hot fluids infiltrating a rock do not necessarily cause equilibration at the cm scale, as has been assumed previously. Simple modelling of solid-state diffusion in mantle minerals shows that isotopic disequilibrium may be preserved for up to hundreds of Myr at mantle lithosphere temperatures (≤1100–1200 °C), unless subsequently affected by transient heating and/or fluid infiltration events. Radiogenic isotope disequilibrium associated with mantle metasomatism may therefore be a common feature of mantle xenoliths.

* Corresponding author at: KiDs (Kimberlites and Diamonds), School of Earth Sciences, The University of Melbourne, Parkville, 3010 Victoria, Australia.
E-mail addresses: andrea.giuliani@mq.edu.au, andrea.giuliani@unimelb.edu.au (A. Giuliani).

https://doi.org/10.1016/j.epsl.2017.11.014
0012-821X/

1. Introduction

Metasomatism, the process by which rocks are modified through interaction with fluids (including melts) of variable composition, can generate new minerals and modify existing phases in mantle rocks (O'Reilly and Griffin, 2013 and references therein). Multiple events of melt extraction and metasomatism have resulted in large geochemical and isotopic variations in the sub-continental lithospheric mantle at every scale (e.g., McDonough and McCulloch, 1987; Pearson et al., 2003; Woodhead et al., 2017). Consequently, understanding how metasomatism operates in the deep Earth and what mineralogical and geochemical changes are produced is important for constraining models of lithosphere evolution and the sources of mantle-derived magmas.

Radiogenic isotope variations are common in metasomatised mantle rocks (e.g., Richardson et al., 1985; Walker et al., 1989; Pearson et al., 1995, 2003). These variations are often generated by radiogenic ingrowth in different phases and, therefore, provide potential chronological constraints on metasomatism or cooling to temperatures below those permissive of isotopic exchange (e.g., Hawkesworth et al., 1990; Carlson and Irving, 1994; Shu et al., 2013, 2014). A link between mantle metasomatism and tectonic/magmatic events recorded in the overlying crust has been occasionally established through radiometric dating of mantle minerals by U/Pb, Sm/Nd and Lu/Hf methods (Kinny and Dawson, 1992; Hamilton et al., 1998; Konzett et al., 1998; Liati et al., 2004; Koornneef et al., 2009; Shu et al., 2013; Giuliani et al., 2014b; Griffin et al., 2014). However, mantle xenoliths derived from the shallow lithospheric mantle (<900–1000 °C) and, occasionally, from deeper, higher temperature domains, commonly show isotopic variations unrelated to radiogenic ingrowth in a closed system (Richardson et al., 1985; Walker et al., 1989; Gunther and Jagoutz, 1994; Pearson et al., 1995; Simon et al., 2007; Koornneef et al., 2009; Aulbach et al., 2013; Shu et al., 2014). Due to the assumption that each metasomatic assemblage is produced by a single fluid of homogeneous composition, these variations are typically attributed to either subsequent metasomatic events prior to or during the magmatic event that transported the xenoliths to surface, or contamination by the magma host (Jagoutz et al., 1980; Pearson et al., 1995; Richardson et al., 1985; Schmidberger et al., 2003; Simon et al., 2007; Aulbach et al., 2013).

Recent studies of kimberlites and entrained xenoliths from the Kimberley kimberlites (South Africa) lead us to question the basic assumption of a single homogeneous metasomatic fluid and suggest that: i) a range of fluids can be generated during a single tectonic/magmatic event in the same mantle domain – e.g., kimberlitic, carbonate, sulfate, Ni-rich C–O–H, and hydrous potassic fluids coeval with kimberlite magmatism in the lithospheric mantle beneath Kimberley (Dawson et al., 2001; Giuliani et al., 2013a, 2013b, 2014a; Konzett et al., 2013; Soltys et al., 2016). ii) Multiple pulses of kimberlite melt precondition the mantle wall rocks lining the magmatic conduit before kimberlite magmas reach the surface (Giuliani et al., 2014a, 2016b). This evidence implies that metasomatism recorded in a single mantle xenolith might result from multiple, perhaps broadly coeval fluids with variable geochemical and isotopic compositions. Therefore, it is possible that isotopic variations in mantle rocks could be an inherent feature of metasomatism in the lithospheric mantle.

In this contribution, we present new SEM images, major–minor element and Sr isotope compositional data for LIMA (LIndsleyite–MAthiasite) titanate and clinopyroxene from three strongly metasomatised peridotite xenoliths from the ~84 Ma Bultfontein kimberlite (Kimberley, South Africa). These results are combined with published LIMA U/Pb ages (Giuliani et al., 2014b) to show that *coeval* fluids with diverse geochemical characteristics contribute to the final metasomatic assemblage produced in a *single* regional event, likely linked to the ~180 Ma Karroo flood basalt province. Therefore, this study provides new insights into the complexity of mantle metasomatic processes and offers an alternative explanation for the common occurrence of isotopic variations in mantle rocks, namely that these variations result from disequilibrium associated directly with metasomatism.

1.1. Overview of LIMA minerals

LIMA minerals are titanates enriched in Cr, Fe and Zr, which contain significant concentrations (100s to 1000s of ppm) of LILE (K, Ba, Sr, Pb), HFSE (Nb, Hf), LREE, U and Th. In the mantle, they typically occur in strongly metasomatised peridotites in close association with other metasomatic phases, including phlogopite, clinopyroxene, K-richterite and ilmenite, where LIMA replace spinel grains (Erlank et al., 1987; Haggerty et al., 1983; Konzett et al., 2013). LIMA grains have also been reported as inclusions in diamonds (Sobolev et al., 1997), and experimental investigations have shown they are stable to depths of ~300 km, i.e. throughout the lithospheric mantle (Konzett et al., 2005). Mantle LIMA minerals are probably produced by silicate or silicate–carbonate melts enriched in HFSE, LILE and LREE (Haggerty et al., 1983; Erlank et al., 1987). The extreme enrichment in incompatible elements and wide P–T stability range identify LIMA minerals as potential source components for mantle-derived alkaline magmas. In the only previous Sr isotope study of LIMA minerals, Griffin et al. (2014) reported initial $^{87}Sr/^{86}Sr$ compositions of between 0.7035–0.7047 for LIMA macrocrysts from the Jagersfontein kimberlite (South Africa), and argued that they formed in the lithospheric mantle broadly coeval with Karoo magmatism. Griffin et al. (2014) attributed this isotopic signature to mixing between a Karoo-related asthenospheric melt and phlogopite-bearing lithospheric mantle.

2. Geological setting and sample description

The three LIMA-bearing peridotite xenoliths (XM1/341, /345 and /362) selected for this study were collected from the Kimberley (South Africa) Boshof Road dumps, which host historical waste material from the Bultfontein kimberlite. The Bultfontein pipe is part of the Kimberley cluster of archetypal kimberlites in the southwestern part of the Kaapvaal Craton (Giuliani et al., 2017). The Bultfontein kimberlite was emplaced at 84.0 ± 0.9 Ma based on phlogopite Rb/Sr dating (Kramers et al., 1983). The initial Sr isotopic composition of the kimberlite magma is 0.70432 ± 0.00005 (2σ), based on *in situ* analyses of carbonate and perovskite grains (Giuliani et al., 2017).

Samples XM1/341 and /362 are coarse-grained, phlogopite-rich lherzolites where phlogopite, clinopyroxene, LIMA and minor Fe–Ni sulfides are in close textural association (Fig. 1; Giuliani et al., 2014b, 2016a). In sample XM1/345, cm-thick, coarse-grained veins of phlogopite with minor ilmenite, LIMA, clinopyroxene and Fe–Ni sulfides occur in a coarse harzburgite matrix. Based on olivine-spinel and clinopyroxene–orthopyroxene thermometry, the samples equilibrated at similar conditions, i.e. $T \sim 800$–900 °C, which correspond to depths of ~100–120 km (Giuliani et al., 2014b).

3. Analytical methods

The micro-textural and compositional variations of LIMA grains were examined by scanning electron microscope (SEM) and electron microprobe (EMP) analyses at the University of Melbourne. Details of the analytical equipment and procedure can be found in Giuliani et al. (2014b).

3.1. In situ Sr isotope determinations

In situ Sr isotope analyses of LIMA and clinopyroxene grains were performed using a 193 nm excimer UV laser ablation probe with Laurin-Technic two volume ablation cell, interfaced with a Nu Plasma multi-collector (MC) ICP-MS. The measurements were performed during 3 distinct analytical sessions in 2011 (LIMA only), 2012 (LIMA and clinopyroxene) and 2014 (additional LIMA). For the 2011 and 2012 sessions, the laser ablation conditions for LIMA analyses were typically: laser fluence <5 mJ cm^{-2}, repetition rate of 5 Hz; beam size of 50–70 μm; ablation time of 50–60 s with sample washout of 30 s; longer delays of 60 s for background measurements were interspersed every 5–10 analyses, and at the beginning and end of each analytical session. Typical signal sizes on Faraday collectors were 1.2–3.0 V of total Sr. The analytical conditions of the 2014 analyses were similar to the previous measurements but, due to improvements in instrumentation, total Sr signal size were considerably higher (7–12 V). The analytical conditions employed to measure the Sr isotope composition of clinopyroxene in 2012 were the same as those used for LIMA grains but the laser repetition rate was higher (6 Hz) and beam size larger (120 μm).

The raw data were reduced using the IOLITE software, which applies corrections for the main isobaric interferences (e.g., ^{87}Rb on ^{87}Sr, doubly-charged Er and Yb on ^{84,86,88}Sr, which occur at levels of 1% or less, and ^{85}Rb, after an on-peak subtraction for Kr – Paton et al., 2007; Woodhead et al., 2005). We employed fragments of modern marine carbonate (MMC, ^{87}Sr/^{86}Sr = 0.70916; Woodhead et al., 2005), perovskite 83P13 (present-day ^{87}Sr/^{86}Sr = 0.70250; Paton et al., 2007) and Ice River perovskite (present-day ^{87}Sr/^{86}Sr = 0.70284; Tappe and Simonetti, 2012) to monitor instrumental performance. Measured values were consistent with accepted values (Supplementary Table S6).

3.2. Solution-mode Rb–Sr isotope analyses

Solution-mode Rb–Sr isotope data were collected for 3 samples of clinopyroxene (XM1/341, /345 and /362) and for 3 samples of LIMA (XM1/341 and 2 for xenolith XM1/362). The handpicked mineral separates (~3 to 9 mg of clinopyroxene, and ~0.1–0.2 mg of LIMA) were cleaned with cold, dilute HCl and distilled water, and dissolved in HF-HNO_3 and HCl on a hot plate (100 °C) over 3–4 days. LIMA grains completely dissolved and the resulting solutions were clear. The solutions were then split for trace element and Sr isotope analyses. Trace element concentrations were determined using the Agilent 7700x ICP-MS housed at the University of Melbourne. Strontium was extracted and purified on a small column of Eichrom Sr resin (0.15 ml of 50–100 mm resin, see Pin et al., 1994), with particular attention paid to removal of Ba from these Ba-rich matrices. Sr isotope analyses were carried out on a Nu Plasma MC-ICP-MS at the University of Melbourne. Sample solutions were introduced via a low-uptake PFA nebulizer and a CETAC Aridus desolvating device and produced total Sr signals of ~6 V. After correction for memory and interference from Rb and Kr (both negligible), Sr isotopic data were corrected for instrumental mass bias by normalizing to ^{88}Sr/^{86}Sr = 8.37521. Possible interference on Sr from $BaAr^{++}$ was monitored at 88.5 and 89 amu and found to be negligible. ^{87}Sr/^{86}Sr results are reported relative to SRM987 ^{87}Sr/^{86}Sr of 0.710230 and have an external precision of ±0.000040 (2σ). Splits of USGS basalt BCR-2, processed and analysed in the same batch, yielded an ^{87}Sr/^{86}Sr ratio of 0.705017 ± 0.000019 (2σ), consistent with TIMS reference data (e.g., Raczek et al., 2003). The ^{87}Rb/^{86}Sr ratios for age corrections are based on the trace element results of the same sample solutions and have precision of ~2% (2σ). The ^{87}Rb decay constant employed for age corrections is 1.3972×10^{-11} (Villa et al., 2015).

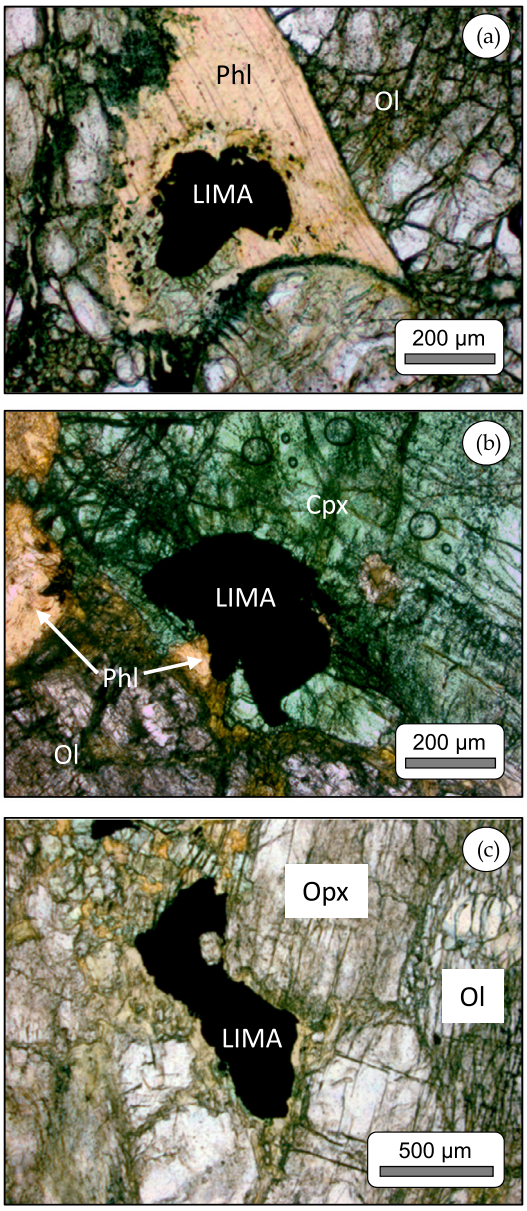

Fig. 1. Optical photomicrographs showing textural details of LIMA grains. (a) LIMA inclusion in phlogopite (Phl); (b) LIMA grain intergrown with clinopyroxene (Cpx) and minor phlogopite; (c) LIMA grain interstitial to orthopyroxene (Opx) and olivine (Ol).

4. Results

LIMA grains occur interstitial to other phases (i.e. olivine, orthopyroxene, clinopyroxene and phlogopite) and as inclusions in, or intergrowths with, phlogopite and clinopyroxene (Fig. 1; Giuliani et al., 2014b). LIMA grains never host inclusions of spinel precursor in these samples. Their size commonly ranges between ~50 and 500 μm (Fig. 2). New and previously published electron microprobe analyses of these LIMA grains show that their compositional features (e.g., high contents of Ti, Cr, Fe and Zr; Figs. 3, 4 and 5; Supplementary Table S1; Giuliani et al., 2014b) are typical of LIMA minerals in mantle xenoliths (Erlank et al., 1987; Haggerty et al., 1983; Konzett et al., 2013). Major element compositions of phlogopite grains are homogeneous within each sample (Giuliani et al., 2016b). Phlogopite in XM1/341 and XM1/345 exhibit similar compositions (TiO_2 = 0.76 ± 0.03 (1sd) and 0.76 ± 0.02 wt.%; Mg# = 90.7 ± 0.4 and 90.9 ± 0.3, respectively),

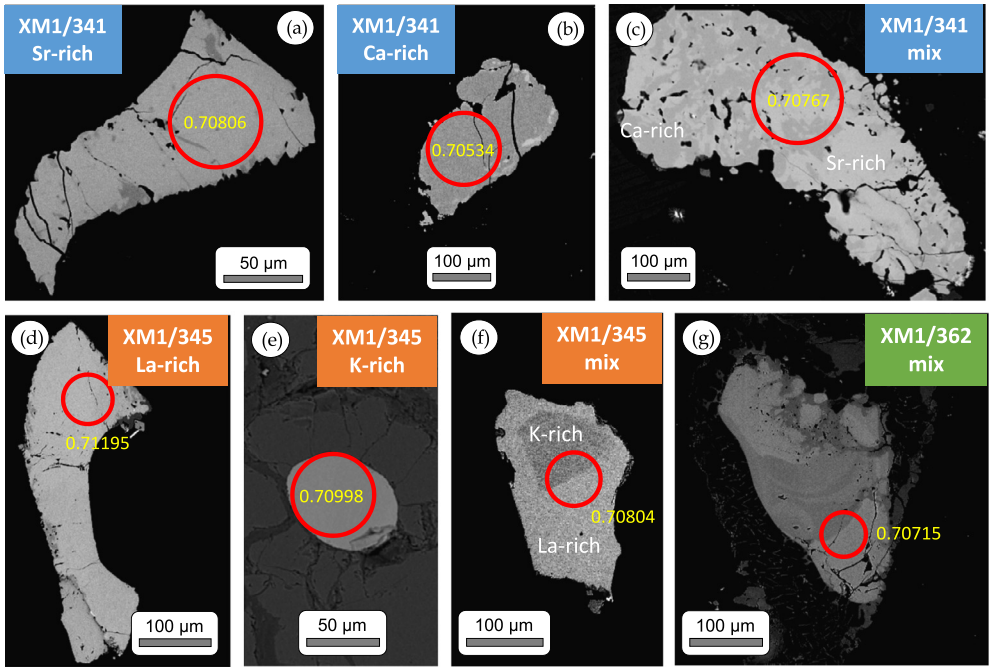

Fig. 2. Scanning-electron microscope (SEM), back-scattered electron (BSE) images of LIMA grains showing their variable composition and internal structure – e.g., intergrowth in panel (c); core of different composition in panel (f); four LIMA types coexisting in the same grain in panel (g). The red circles show the location of laser spots for Sr isotope analysis and include the associated measured $^{87}Sr/^{86}Sr$ ratios. (For interpretation of the references to colour in this figure legend, the reader is referred to the web version of this article.)

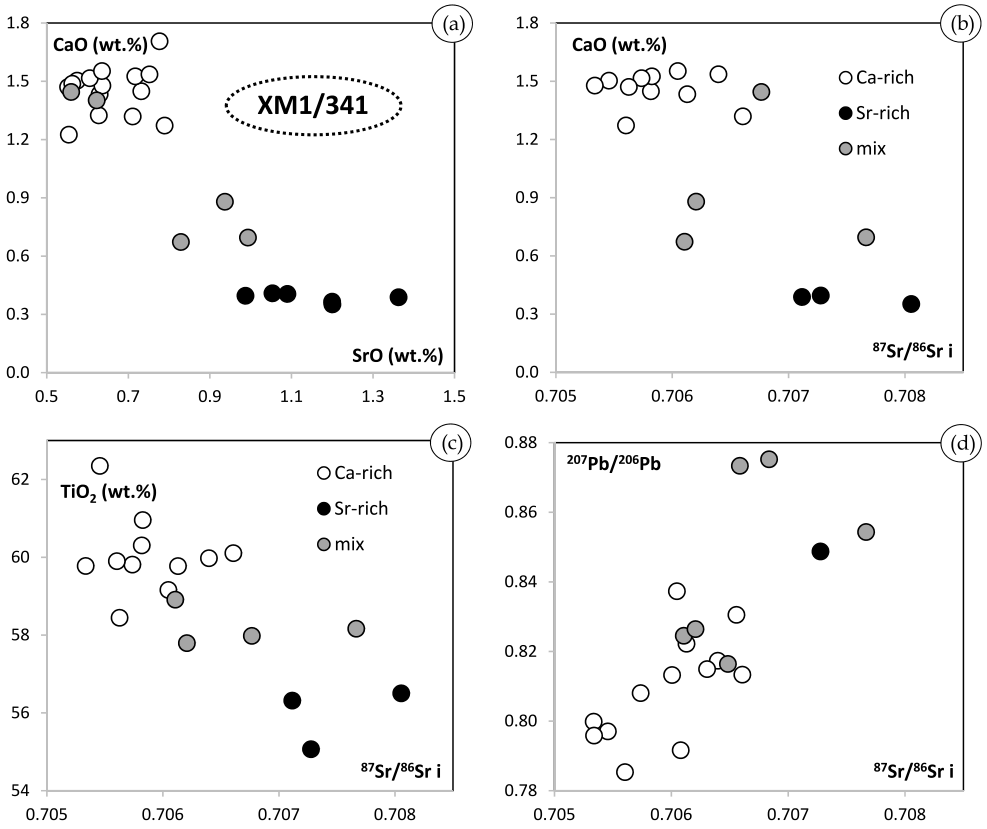

Fig. 3. Major element, Sr and Pb isotope (measured *in situ*) covariation diagrams of LIMA grains in xenolith sample XM1/341. The term 'mix' indicates analyses with contributions from different LIMA types (i.e. 'Ca-rich' and 'Sr-rich'). Initial Sr isotope values ('$^{87}Sr/^{86}Sr$ i') calculated using the age of LIMA formation (177 ± 12 Ma) from Giuliani et al. (2014b). $^{207}Pb/^{206}Pb$ ratios are from Giuliani et al. (2014b). The complete dataset is available in Supplementary Table S5.

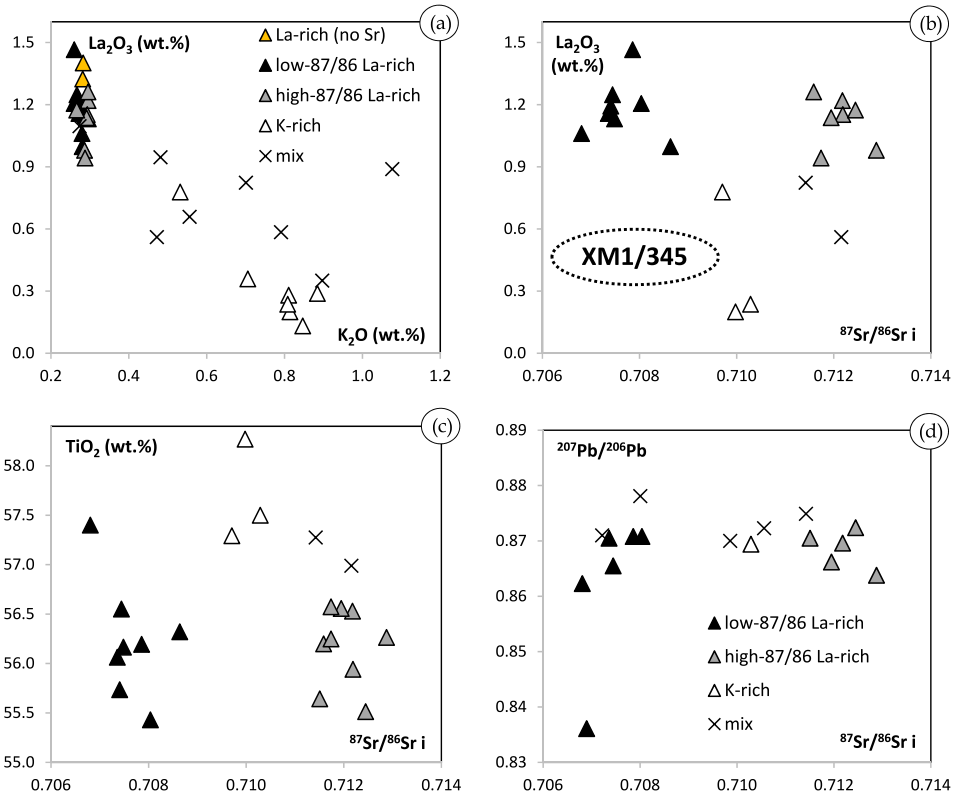

Fig. 4. Major element, Sr and Pb isotope (measured *in situ*) covariation diagrams of LIMA grains in xenolith sample XM1/345. The term 'mix' indicates analyses with contributions from different LIMA types (i.e. 'K-rich', 'low-$^{87}Sr/^{86}Sr$ La-rich' and 'high-$^{87}Sr/^{86}Sr$ La-rich'). In panel (a) 'La-rich (no Sr)' denotes grains where Sr isotope composition was not measured. Initial Sr isotope values ('$^{87}Sr/^{86}Sr$ i') calculated using the age of LIMA formation (178 ± 29 Ma) from Giuliani et al. (2014b). $^{207}Pb/^{206}Pb$ ratios are from Giuliani et al. (2014b). The complete dataset is available in Supplementary Table S5.

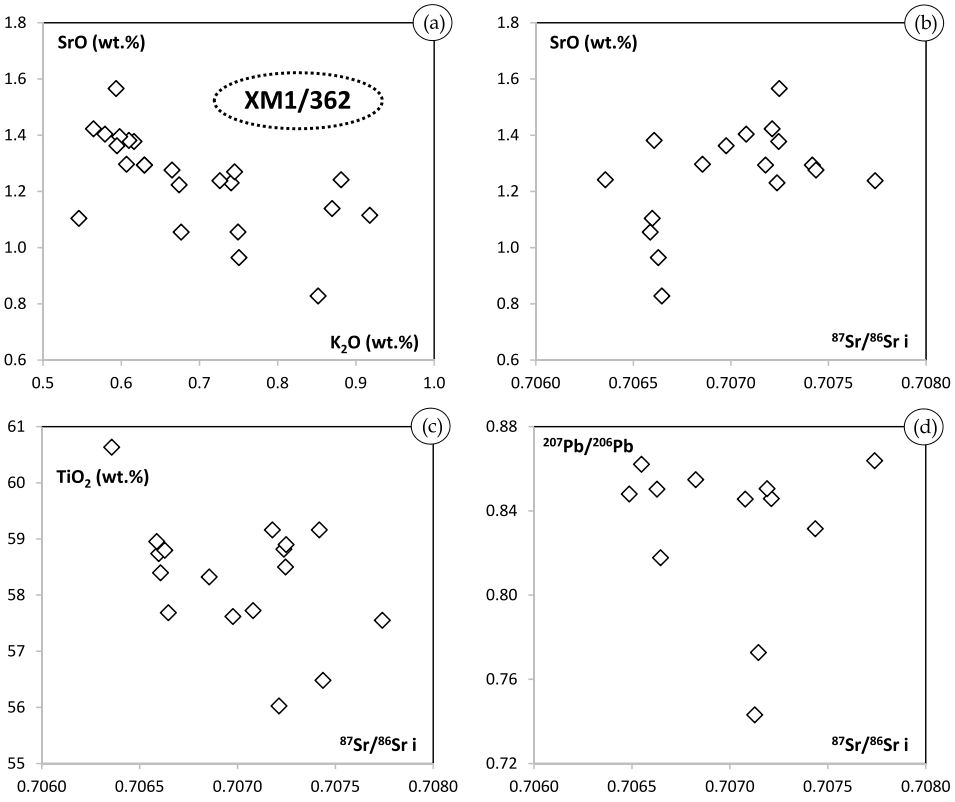

Fig. 5. Major element, Sr and Pb isotope (measured *in situ*) covariation diagrams of LIMA grains in xenolith sample XM1/362. Initial Sr isotope values ('$^{87}Sr/^{86}Sr$ i') calculated using the age of LIMA formation (190 ± 24 Ma) from Giuliani et al. (2014b). $^{207}Pb/^{206}Pb$ ratios are from Giuliani et al. (2014b). The complete dataset is available in Supplementary Table S5.

Table 1
Comparison between solution-mode and in-situ Sr isotope measurements of LIMA and clinopyroxene from xenolith samples XM1/341, /345 and /362.

Sample	Label	Solution mode							In situ				
		Weight (mg)	Rb (ppm)	Sr (ppm)	$^{87}Sr/^{86}Sr$ measured[a]	$^{87}Rb/^{86}Sr$	Age (Ma)[b]	$^{87}Sr/^{86}Sr$ initial	Variation	$^{87}Sr/^{86}Sr$ initial		MSWD	*n*
										range	*weighted mean*		
XM1/341	341 clinopyroxene	8.6	0.84	638	0.70787	0.0038	177	0.70786	no		0.7081 ± 0.0002	0.95	15
	341 LIMA	0.21	7.89	6108	0.70705	0.0037	177	0.70704	yes	0.7053–0.7082	0.7069 ± 0.0002	523	56
	Ca-rich LIMA									0.7053–0.7066	0.7059 ± 0.0004[c]		20
	Sr-rich LIMA									0.7071–0.7081	0.7075 ± 0.0005[c]		3
XM1/345	345 clinopyroxene	3.2	1.99	561	0.71168	0.0103	178	0.71166	yes	0.7091–0.7129	0.7107 ± 0.0009	26	12
	low-$^{87}Sr/^{86}Sr$ Cpx									0.7090–0.7100	0.7096 ± 0.0003[c]		5
	high-$^{87}Sr/^{86}Sr$ Cpx									0.7121–0.7129	0.7126 ± 0.0003[c]		4
	345 LIMA	–	–	–	–	–			yes	0.7068–0.7131	0.7104 ± 0.0008	2181	39
	K-rich LIMA									0.7097–0.7103	0.7100 ± 0.0003[c]		3
	low-$^{87}Sr/^{86}Sr$ La-rich LIMA									0.7068–0.7086	0.7076 ± 0.0006[c]		9
	high-$^{87}Sr/^{86}Sr$ La-rich LIMA									0.7115–0.7129	0.7120 ± 0.0004[c]		9
XM1/362	362 clinopyroxene	7.6	2.81	518	0.70694	0.0157	190	0.70690	no		0.7077 ± 0.0003	0.20	11
	362 LIMA 1	0.14	3.78	12984	0.70680	0.0008	190	0.70680	yes	0.7064–0.7077	0.7071 ± 0.0002	55	25
	362 LIMA 2	0.09	3.41	12300	0.70680	0.0008	190	0.70679					

[a] External reproducibility (±2 sd) of 0.00004.
[b] LIMA U/Pb ages (Giuliani et al., 2014b).
[c] Mean ± standard deviation.

whereas XM1/362 phlogopite is marginally richer in Ti, Mg and Al (TiO_2 = 1.0 ± 0.2 wt.%; Mg# = 93.3 ± 0.1).

4.1. XM1/341

SEM-BSE images of LIMA grains in sample XM1/341 show that two compositionally distinct types of LIMA (i.e., 'Ca-rich' and 'Sr-rich'; Fig. 2a, b) occur in this sample, and are frequently intergrown (Fig. 2c). The major element compositions ($n = 35$; Fig. 3a) form a major cluster at high CaO and relatively low SrO concentrations (1.4 ± 0.1 and 0.7 ± 0.1 (1σ) wt.%, respectively), with a smaller group at lower CaO (<0.4 wt.%) and higher SrO contents (>1.7 wt.%). Some grains that contain Ca-rich and Sr-rich zones have EMP compositions overlapping the Ca-rich group, while others show intermediate compositions due to inclusion of Ca-rich and Sr-rich types in the X-ray excitation volumes.

SEM-BSE images were used to identify Ca- and Sr-rich zones of sufficiently large size for laser ablation MC-ICPMS analysis (i.e. >60–70 µm; Fig. 2a, b, c). $^{87}Sr/^{86}Sr$ compositions of the two LIMA types are distinct, i.e. 0.7053–0.7066 for Ca-rich LIMA; >0.7071 for the 3 measured Sr-rich grains (Fig. 3, Table 1 and Supplementary Table S3 and S5). Analyses of mixed Ca and Sr-rich domains produced intermediate values that marginally overlap the compositional fields of Ca-rich and Sr-rich LIMA. The low $^{87}Rb/^{86}Sr$ ratios of LIMA (typically <0.004) in all xenolith samples imply that measured and initial $^{87}Sr/^{86}Sr$ ratios (i.e., at the time of metasomatism) are within uncertainty (Table S3). $^{87}Sr/^{86}Sr$ values for all grains measured in sample XM1/341 ($n = 56$; including grains not measured by EMP) are characterised by a major mode between 0.7060–0.7065 (i.e. in the range of Ca-rich LIMA) with a long tail towards higher values typical of Sr-rich LIMA (Fig. 6a). LIMA $^{87}Sr/^{86}Sr$ ratios broadly correlate with major oxide concentrations (Fig. 3b, c) and $^{207}Pb/^{206}Pb$ ratios (Fig. 3d). The end members of these trends are Ca- and Sr-rich LIMA phases, with intermediate compositions represented by analyses of intergrown LIMA (and some Ca-rich grains with minor Sr-rich components). These correlations probably reflect physical entrainment of different LIMA types during EMP and/or laser ablation analyses.

XM1/341 clinopyroxene grains are characterised by homogeneous major element composition (Mg# = 90.8 ± 0.3 (1σ); CaO = 21.6 ± 0.3 wt.%; Cr_2O_3 = 2.1 ± 0.1 wt.%; $n = 16$; Table S2). *In situ* Sr isotope analyses show limited variations with a weighted average composition of 0.7081 ± 0.0002 (2σ, $n = 15$; Table 1 and S4). This composition overlaps the most radiogenic values of LIMA grains (Fig. 6a), i.e. the Sr-rich LIMA group.

4.2. Sample XM1/345

SEM examination of this sample shows that two types of LIMA (i.e. 'La-rich' and 'K-rich') coexist as single homogeneous grains or compositionally distinct zones in the same grain (Fig. 2d, e, f). K-rich domains occasionally occur at the core of La-rich LIMA grains (Fig. 2f). EMP analyses ($n = 47$) confirm that the La- and K-rich LIMA phases, identified by means of SEM-BSE images, have distinct compositions (i.e. La_2O_3 = 1.2 ± 0.3 *vs* 0.3 ± 0.1 wt.%; K_2O = 0.28 ± 0.01 *vs* 0.82 ± 0.09 wt.%; Fig. 4a). Major element compositions intermediate between the two LIMA types are attributed to inclusion of La- and K-rich domains in the X-ray excitation volumes of EMP analyses.

In situ Sr isotope determinations on LIMA grains selected using SEM-BSE images reveal additional complexity. La-rich LIMA phases can be separated into two groups with significantly different $^{87}Sr/^{86}Sr$ compositions, i.e. <0.7080 and >0.7115 (Fig. 4b, c; Table 1 and Table S5). The three measured K-rich LIMA have $^{87}Sr/^{86}Sr$ ratios (0.7097–0.7103) intermediate between the two La-rich groups. $^{87}Sr/^{86}Sr$ values for all measured grains ($n = 38$; in-

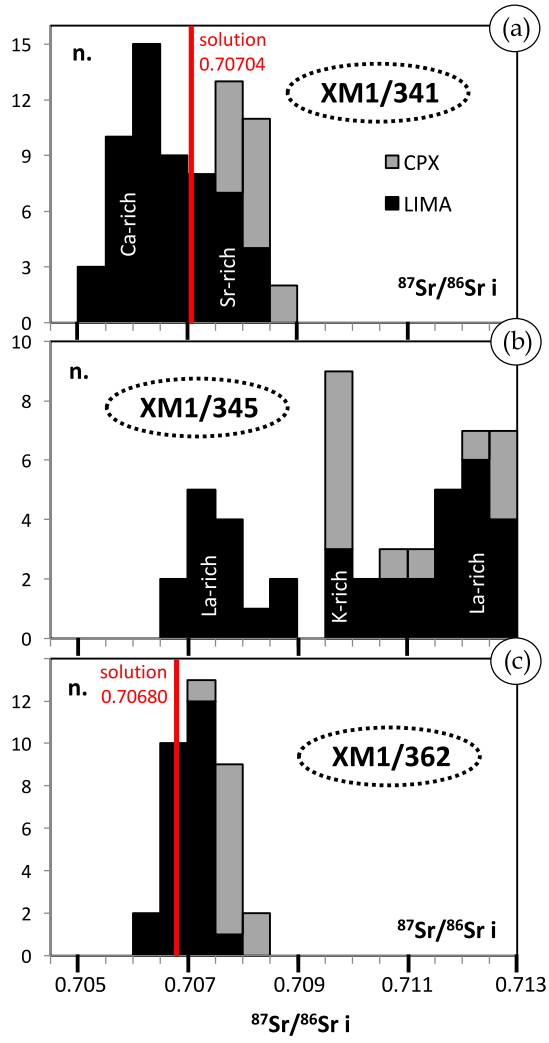

Fig. 6. Distribution of Sr isotope compositions measured *in situ* for LIMA and clinopyroxene grains in xenolith samples XM1/341 (a), /362 (b) and /345 (c). The Sr isotope compositions of each LIMA type (i.e., 'Ca-rich' and 'Sr-rich' in panel a; 'K-rich' and 'La-rich' in panel b) are inferred from Figs. 3 and 4. Red lines indicate the Sr isotope values measured by solution mode. Initial Sr isotope values ('$^{87}Sr/^{86}Sr$ i') calculated using the age of LIMA formation from Giuliani et al. (2014b). The complete dataset is available in Supplementary Table S3 (LIMA) and S4 (clinopyroxene). (For interpretation of the references to colour in this figure legend, the reader is referred to the web version of this article.)

cluding grains not analysed by EMP) occupy two major modes at ~0.7070–0.7080 and 0.7115–0.7130 (Fig. 6b), which correspond to the two La-rich groups. A third minor mode at 0.7095–0.7100 represents the K-rich type. There is limited variability in $^{207}Pb/^{206}Pb$ ratios across the three LIMA types (i.e. 'K-rich', 'low-$^{87}Sr/^{86}Sr$ La-rich' and 'high-$^{87}Sr/^{86}Sr$ La-rich'; Fig. 4d).

In contrast to the other samples, clinopyroxene grains in xenolith XM1/345 show distinct compositional variations. Cr_2O_3 concentrations (1.2–2.1 wt.%) are directly correlated with Na_2O contents (Fig. 7a), and inversely correlated with $^{87}Sr/^{86}Sr$ ratios (Fig. 7b). Conversely, CaO concentrations (22.8 ± 0.2 wt.%) and Mg# values (92.2 ± 0.1) do not vary (Table S3) and differ from the composition of XM1/341 clinopyroxene. The $^{87}Sr/^{86}Sr$ ratios of clinopyroxene grains range between 0.7091 and 0.7129 ($n = 12$; Table 1 and S4), with two major modes at 0.7090–0.7100 ($n = 5$) and 0.7120–0.7130 ($n = 4$). These compositions broadly overlap those of K-rich and high-$^{87}Sr/^{86}Sr$ La-rich LIMA phases, respectively (Fig. 6b).

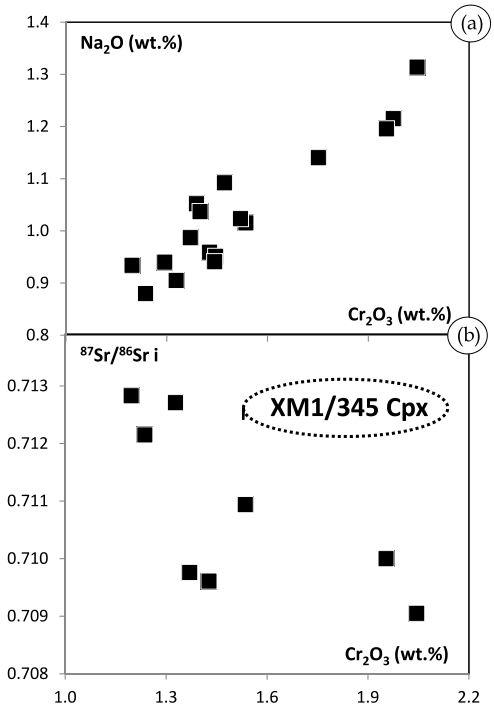

Fig. 7. Major element and Sr isotope (measured *in situ*) covariation diagrams of clinopyroxene grains in xenolith sample XM1/345. Initial Sr isotope values ('$^{87}Sr/^{86}Sr$ i') calculated assuming clinopyroxene formation coeval with LIMA and using the age of LIMA crystallisation (178 ± 29 Ma) from Giuliani et al. (2014b).

4.3. XM1/362

In this sample LIMA grains consist of at least four compositionally distinct zones, which could only be resolved by SEM-BSE observation (Fig. 2g). Major element compositions show variations between high Sr (low K) and low Sr (high K) compositions (Fig. 5a). $^{87}Sr/^{86}Sr$ ratios measured *in situ* do not correlate with major element concentrations (Fig. 5b, c) or $^{207}Pb/^{206}Pb$ ratios (Fig. 5d). The lack of correlation may be due to different sampling volumes of the analytical techniques (i.e. beam size of ~2 μm for EMPA *vs* 50–70 μm for LA-MC-ICPMS), coupled with fine-scale mingling of different LIMA types in the grains examined (Fig. 2g). The Sr isotope compositions show a normal distribution with a single mode at ~0.707 ($n = 25$; Fig. 6c).

XM1/362 clinopyroxene grains show no measurable compositional variations (Mg# = 91.2 ± 0.2 (1σ); CaO = 20.1 ± 0.3 wt.%; Cr_2O_3 = 3.3 ± 0.3 wt.%; $n = 7$; Table S2), and have different major element concentrations compared to clinopyroxene in samples XM1/341 and XM1/345. The $^{87}Sr/^{86}Sr$ composition measured by LA-MC-ICPMS (0.7077 ± 0.0003 (2σ); $n = 11$; Table S4) overlaps the most radiogenic values of LIMA grains (Fig. 6c).

4.4. In situ vs solution Sr isotope analyses

To validate the *in situ* Sr isotope analytical protocol adopted in this study, the isotopic compositions of LIMA and clinopyroxene were also determined by solution MC-ICPMS methods. The LIMA solution analyses are within the range of $^{87}Sr/^{86}Sr$ compositions measured by laser ablation, and similar to the weighted means of *in situ* analyses (Table 1). In a study of LIMA macrocrysts from the Jagersfontein kimberlite (South Africa), Griffin et al. (2014) similarly obtained overlapping Sr isotope compositions for individual grains measured by *in situ* and solution methods. The $^{87}Sr/^{86}Sr$ compositions of XM1/341 and /362 clinopyroxene determined by solution methods are within uncertainty (XM1/341), or in close proximity (<0.0003; XM1/362), to the weighted means of

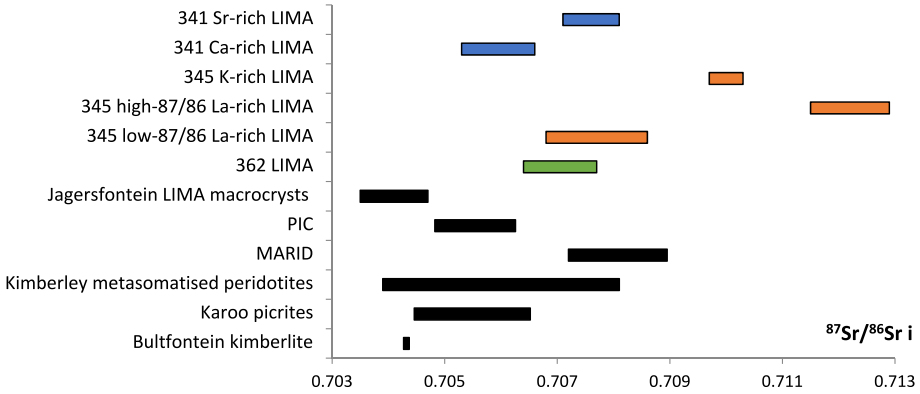

Fig. 8. Initial $^{87}Sr/^{86}Sr$ variations of LIMA phases in samples XM1/341 and XM1/345, and LIMA grains in sample XM1/362 compared to LIMA macrocrysts from the Jagersfontein kimberlite in South Africa (Griffin et al., 2014); PIC (phlogopite-ilmenite-clinopyroxene) and MARID (mica-amphibole-rutile-ilmenite-diopside) rocks from the Kimberley area (Giuliani et al., 2013b, 2015 and references therein); modally metasomatised peridotites from the Kimberley kimberlites (Kramers et al., 1983; Richardson et al., 1985; Hawkesworth et al., 1990; Gunther and Jagoutz, 1994); Karoo picrites (georoc.mpch-mainz.gwdg.de); and the Bultfontein kimberlite (Giuliani et al., 2017). Initial isotopic values for PIC, MARID and metasomatised peridotites are calculated using the emplacement age of the Bultfontein kimberlite (84 Ma; Kramers et al., 1983). 'PIC' includes analyses previously referred to as 'depleted MARID' (Giuliani et al., 2015).

LA-MC-ICPMS analyses. Considering minor natural variations, for example induced by interaction with or contamination by kimberlite melts/fluids (e.g., Richardson et al., 1985; Schmidberger et al., 2003), these similarities demonstrate the robustness of the *in situ* results.

5. Discussion

5.1. LIMA formation from compositionally distinct fluids

In each sample examined in this study, LIMA minerals show variable elemental and Sr isotope compositions (Figs. 3, 4, 5 and 6). We consider it unlikely that the variation is associated with diffusion across the boundaries between LIMA types as SEM-BSE images show very sharp boundaries between compositionally distinct LIMA phases coexisting in the same grain (Fig. 2). This conclusion is reached despite the examined LIMA grains residing in the lithospheric mantle at T of ~800–900 °C for ~100 Myr, i.e. between the times of metasomatism at ~180–190 Ma (Giuliani et al., 2014b) and kimberlite emplacement at ~84 Ma (Kramers et al., 1983).

In sample XM1/341, several LIMA grains consist of finely intergrown Ca- and Sr-rich LIMA phases, with some grains dominated by one compositional type (Fig. 2a, b, c). Each LIMA type shows a distinct and well-defined elemental, Sr and, perhaps, Pb isotope composition (Fig. 3). This requires two discrete episodes of LIMA formation involving fluids with different compositions. The intergrowth structure of XM1/341 LIMA grains, coupled with the preservation of distinct Sr isotope compositions, suggests partial overprinting of an earlier LIMA generation by a later fluid rather than mixing of different fluids. The $^{87}Sr/^{86}Sr$ composition of clinopyroxene overlaps that of Sr-rich LIMA (Fig. 6a and Table 1). This suggests that clinopyroxene was introduced together with Sr-rich LIMA, or alternatively, a previous generation of clinopyroxene, perhaps coeval with Ca-rich LIMA, was entirely overprinted during subsequent metasomatism.

Peridotite XM1/345 contains three generations of LIMA: K-rich; low-$^{87}Sr/^{86}Sr$ La-rich; and high-$^{87}Sr/^{86}Sr$ La-rich (Figs. 2 and 4). The most striking feature of this sample is the identical major element composition of the two La-rich LIMA types that have distinct $^{87}Sr/^{86}Sr$ ratios (i.e. ~0.7070–0.7080 and 0.7115–0.7130; Fig. 4b, c, and Table 1). Diffusion of radiogenic Sr from phlogopite could increase the $^{87}Sr/^{86}Sr$ ratios of LIMA because phlogopite, due to its high Rb/Sr of 236 ± 44 (Giuliani et al., 2016b), could develop highly radiogenic Sr isotope composition during the ~100 Myr of mantle residence after metasomatism. Both low-$^{87}Sr/^{86}Sr$ La-rich and high-$^{87}Sr/^{86}Sr$ La-rich LIMA types, however, occur in contact with phlogopite, which implies that the Sr isotope difference between the two LIMA types could not originate from diffusion of radiogenic Sr from phlogopite. It therefore appears that sample XM1/345 experienced three separate episodes of LIMA crystallisation. The occurrence of K-rich LIMA at the core of grains dominated by the La-rich component (both low- and high-$^{87}Sr/^{86}Sr$; e.g., Fig. 2f) suggests that K-rich LIMA formed before La-rich LIMA. Among the examined grains, we did not observe the two types of La-rich LIMA coexisting, which prevents an assessment of their order of crystallisation. The $^{87}Sr/^{86}Sr$ ratios of XM1/345 clinopyroxene grains cluster in two groups coinciding with the values of K-rich and high-$^{87}Sr/^{86}Sr$ La-rich LIMA, respectively (Fig. 6b and Table 1). This indicates crystallisation of clinopyroxene during at least two episodes of LIMA formation. Some clinopyroxene grains exhibit isotopic compositions intermediate between the two end members, which might be due to partial overprinting of the earlier population (i.e. coeval with K-rich LIMA) during later metasomatism that introduced high $^{87}Sr/^{86}Sr$ La-rich LIMA minerals and clinopyroxene. A similar example of partial metasomatic modification of the Sr isotope compositions of clinopyroxene grains in mantle xenoliths was reported by Schmidberger et al. (2003) for samples from the Nikos kimberlite (Somerset Island, Canada).

Peridotite XM1/362 hosts four LIMA types (Fig. 2), where major element, Sr and Pb isotope compositions could not be clearly resolved (Fig. 5). The Sr isotope composition of clinopyroxene grains overlaps the most radiogenic LIMA values of sample XM1/362 (Fig. 6c), perhaps providing the isotopic signature of one of the LIMA-forming fluids.

In summary, the examined samples preserve evidence of up to three and, perhaps, four distinct episodes of LIMA (± clinopyroxene and, probably, phlogopite and sulfide) formation in each xenolith. LIMA metasomatism was probably triggered by alkaline mafic melts enriched in HFSE (e.g., Ti, Zr, Nb), LILE (Ba, Sr, Pb) and LREE (Haggerty et al., 1983; Erlank et al., 1987; Giuliani et al., 2014b). There is no evidence that the compositional variations between coexisting LIMA types are related to partial re-equilibration with phlogopite or other phases. In addition, no LIMA group overlaps the unradiogenic Sr isotope composition of the Bultfontein kimberlite (~0.7043; Giuliani et al., 2017) (Fig. 8); and the U/Pb systematics of LIMA minerals was not perturbed during kimberlite magmatism and xenolith transport to surface (Giuliani et al., 2014b). This implies that the LIMA grains did not interact ma-

terially with the kimberlite magma that entrained the examined samples.

5.2. Origin of LIMA-forming fluids

LIMA minerals in samples XM1/341 (i.e. Ca- and Sr-rich) and XM1/345 (K-rich, low- and high-$^{87}Sr/^{86}Sr$ La-rich) form compositionally distinct groups, some in Sr isotope equilibrium with clinopyroxene (i.e., Sr-rich LIMA in XM1/341; K-rich and high-$^{87}Sr/^{86}Sr$ La-rich LIMA in XM1/345). There are, however, significant elemental and Sr isotope variations within each LIMA group (commonly >0.001 $^{87}Sr/^{86}Sr$; Figs. 3 and 4, Table 1), which far exceed the analytical uncertainties (e.g., <0.0003 for $^{87}Sr/^{86}Sr$ measurements; Table S3). Part of this variation is probably due to the heterogeneous composition of several LIMA grains, which commonly include rims, veins or zones with distinct compositions (e.g., Fig. 2a, b). Other factors that may have contributed to the compositional heterogeneity of each LIMA group include i) fluid evolution during interaction with the mantle protolith, ii) variable assimilation of wall rock material coupled with fractionation during fluid ascent before metasomatism, iii) fractional melting of a heterogeneous source, iv) fluid mixing, and v) partial overprinting during subsequent metasomatic events. Evidence of small-scale fluid evolution is supported by a previous study of a strongly metasomatised mantle xenolith from Bultfontein, where LIMA grains show discontinuous core-to-rim zoning towards decreasing K and increasing Ba contents (Konzett et al., 2013). Variable contribution from wall rock assimilation may be consistent with Sr–Nd isotope data for LIMA macrocrysts from the Jagersfontein kimberlite (South Africa), which exhibit compositions trending towards those of the enriched subcontinental lithospheric mantle (i.e., high $^{87}Sr/^{86}Sr$ and low $^{143}Nd/^{144}Nd$ ratios; Griffin et al., 2014). LIMA interactions with later fluids are also possible given the extensive evidence of mantle metasomatism coeval with ~80–90 Ma kimberlite and ~115–120 Ma orangeite magmatism in the area (Hawkesworth et al., 1990; Kinny and Dawson, 1992; Hamilton et al., 1998; Konzett et al., 1998, 2013; Simon et al., 2007; Giuliani et al., 2013a, 2013b, 2014a; Soltys et al., 2016). The effects of later metasomatism on LIMA Pb isotopes must be minimal because LIMA preserve meaningful U/Pb ages, which are consistent with U/Pb age constraints provided by coexisting zircon (Giuliani et al., 2014b).

The Sr isotope compositions of Ca- and Sr-rich LIMA in XM1/341, low-$^{87}Sr/^{86}Sr$ La-rich LIMA in XM1/345 and LIMA in XM1/362, overlap the range shown by modally metasomatised peridotites from the Kimberley kimberlites, including MARID (mica-amphibole-rutile-ilmenite-diopside) rocks (Fig. 8; Kramers et al., 1983; Richardson et al., 1985; Hawkesworth et al., 1990; Gunther and Jagoutz, 1994; Giuliani et al., 2013b, 2015 and references therein). In contrast, K-rich and high-$^{87}Sr/^{86}Sr$ La-rich LIMA minerals in XM1/345 show Sr isotope ratios beyond those previously documented for mantle xenoliths from the Kimberley area (Fig. 8). The elevated $^{87}Sr/^{86}Sr$ ratios of XM1/345 K-rich (0.7097–0.7103) and high-$^{87}Sr/^{86}Sr$ La-rich (0.7115–0.7129) LIMA phases suggest LIMA formation in a previously metasomatised phlogopite-rich protolith or, in alternative, fluid interaction with enriched lithospheric mantle or subducted crustal material recycled in the mantle. Involvement of recycled crustal material is consistent with the S isotope systematics (i.e. $\delta^{34}S = -2$ to $-6‰$) of sulfides in sample XM1/345 (Giuliani et al., 2016a).

XM1/341 Ca-rich LIMA represents the only LIMA phase where Sr isotope ratios resemble those of Karoo picrites (Fig. 8). These picrites probably best approximate the composition of the plume that generated the Karoo large igneous province at ~180 Ma. The temporal relationship between LIMA metasomatism and Karoo magmatism (Giuliani et al., 2014b) coupled with the radiogenic isotopic compositions of LIMA minerals, ranging from Karoo magmas to enriched lithospheric mantle, suggest LIMA derivation from complex interaction between Karoo-related fluids and lithospheric mantle rocks. A similar origin was proposed by Griffin et al. (2014) to explain the formation of LIMA macrocrysts from the Jagersfontein kimberlite. The $^{87}Sr/^{86}Sr$ ratios of Jagersfontein LIMA minerals, however, extend to significantly lower values (down to 0.7035) than Karoo picrites and LIMA minerals in Bultfontein mantle xenoliths (Fig. 8). This evidence probably requires the involvement of other asthenospheric fluids (or depleted lithospheric components) in the formation of the Jagersfontein LIMA macrocrysts. Finally, although the LIMA grains from Jagersfontein show $^{87}Sr/^{86}Sr$ ratios similar to those of southern African Cretaceous kimberlites (e.g., 0.70445 ± 0.00028 for the Jagersfontein kimberlite; Woodhead et al., 2009), the U/Pb age of these LIMA is significantly older (162 ± 46 Ma) and their genesis therefore unrelated to kimberlite magmatism.

5.3. Isotopic disequilibrium associated with mantle metasomatism

In each peridotite, LIMA grains plot along a single regression line in $^{207}Pb/^{206}Pb$ vs $^{206}Pb/^{238}U$ diagrams, corresponding to ages broadly coeval with the ~180 Ma Karoo magmatic event (177 ± 12, 178 ± 29, and 190 ± 24 Ma for samples XM1/341, /345 and /362, respectively; Giuliani et al., 2014b). The large uncertainties associated with the LIMA ages are due to scatter about the regression lines, and might therefore indicate fluid infiltration and attendant LIMA formation over some Myr. The temporal link between mantle metasomatism and Karoo magmatism is, however, robust because the emplacement of Karoo magmas was the only major tectonic/magmatic event at the time.

The combination of major element, Sr and U–Pb isotope compositions of LIMA minerals demonstrate that mantle metasomatic assemblages, seemingly generated during the same geological event (i.e., Karoo magmatism in this case), may result from the infiltration of multiple, broadly coeval fluids. Comparison between the elemental and Sr isotope compositions of different LIMA generations in samples XM1/341 and XM1/345 (Fig. 9 and Table S5) shows that each LIMA type is characterised by a distinct composition. The only exceptions might be XM1/341 Sr-rich and XM1/345 low-$^{87}Sr/^{86}Sr$ La-rich LIMA, which show broadly similar compositions at marginally different Zr (Fig. 9d) and LREE contents (not shown). Metasomatism of these two xenoliths by a similar fluid is possibly supported by the overlapping phlogopite compositions in XM1/341 and /345. Each LIMA-forming fluid was characterised by a different geochemical signature despite being able to produce (or equilibrate with) the same mineralogical assemblage. This is reminiscent of the highly variable $^{87}Sr/^{86}Sr$ ratios of coeval fluid inclusions in fibrous diamonds from Botswana (up to ~0.008 difference for the same diamond, coupled with low Rb/Sr; Klein-BenDavid et al., 2010). These variations were attributed to small-scale mixing between an asthenospheric component with unradiogenic Sr and a high-$^{87}Sr/^{86}Sr$ fluid derived from phlogopite-rich lithologies in the lithospheric mantle (Klein-BenDavid et al., 2010). The compositional variations between distinct LIMA types in the <20 km of mantle domain (100 to 120 km of depth recorded by the studied xenoliths) beneath Kimberley, may be explained by a similar process to that inferred by Klein-BenDavid et al. (2010). An alternative explanation is that a range of fluid compositions were generated from one or more parental fluids during migration via progressive equilibration with wall rocks (i.e. reactive porous flow; e.g., Ionov et al., 2002).

Rb–Sr, Sm–Nd and Lu–Hf isotope heterogeneity at the time of transport to the surface is common in mantle xenoliths equilibrated at low temperature (<900–1000 °C; e.g., Richardson et al., 1985; Gunther and Jagoutz, 1994; Pearson et al., 1995). Similar heterogeneity is also present in high-temperature (>1000 °C)

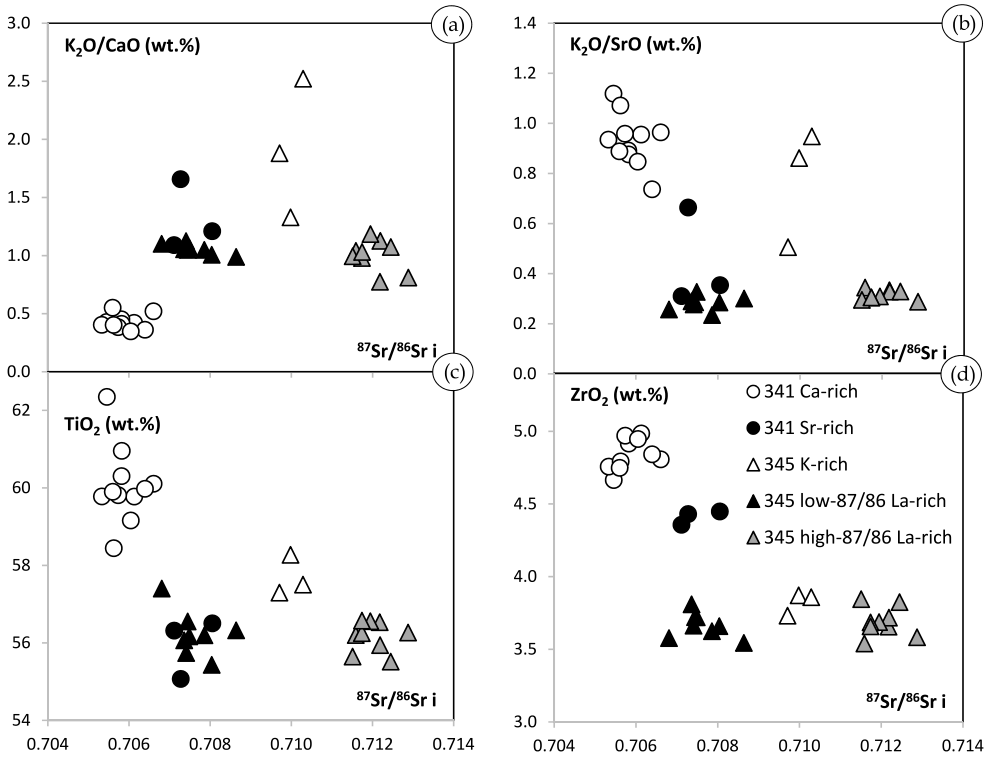

Fig. 9. Sr isotope vs major element covariation diagrams comparing LIMA types in xenolith samples XM1/341 and XM1/345. Initial Sr isotope values ('$^{87}Sr/^{86}Sr$ i') calculated using the age of LIMA formation from Giuliani et al. (2014b).

mantle rocks (Schmidberger et al., 2003; Koornneef et al., 2009; Aulbach et al., 2013; Shu et al., 2014 and references therein). Isotopic variations are generally attributed to i) radiogenic ingrowth, ii) metasomatic overprinting, iii) diffusive re-equilibration after mineral formation during residence in the mantle, iv) interaction with (or contamination by) the entraining magma, or v) combinations thereof (Richardson et al., 1985; Walker et al., 1989; Carlson and Irving, 1994; Pearson et al., 1995; Schmidberger et al., 2003; Simon et al., 2007; Aulbach et al., 2013; Shu et al., 2013, 2014). The geochemical complexity revealed by *in situ* analyses of LIMA minerals suggests an additional mechanism, i.e. isotopic disequilibrium as an inherent feature of metasomatism, when multiple, broadly coeval fluids with variable composition contribute to the final metasomatic assemblage. In the shallow lithosphere, for example at conditions below ~850–950 °C, which Shu et al. (2014) estimated as the closure temperature of the Sm–Nd and Lu–Hf isotope systems, it is likely that the small-scale geochemical heterogeneities introduced during metasomatism will essentially 'freeze in' unless disturbed by subsequent thermal perturbations. The LIMA-bearing peridotites examined in this study, which equilibrated at ~800–900 °C, support this inference. In high-temperature rocks (i.e. >1000 °C), the preservation of isotopic disequilibrium will depend on the scale of metasomatic modification, fluid availability, temperature and time between metasomatism and transport to cooler regions. Solid-state diffusion of REE, including neodymium, is slow in clinopyroxene (Van Orman et al., 2001), orthopyroxene (Cherniak and Liang, 2007), olivine (Chakraborty, 2010) and, to a lesser extent, garnet (Van Orman et al., 2002) at mantle conditions (e.g., 1 mm diffusion in clinopyroxene and garnet at 1100 °C and ~3 GPa takes ~2.0 Gyr and 13 Myr, respectively). Strontium diffusion in diopside is significantly faster and the only available formulation (Sneeringer et al., 1984) shows that at $T \geq 1100$ °C, Sr isotope homogenisation at the grain scale (~1 mm) is achieved in <15,000 yr. Strontium diffusion in peridotitic mantle is, however, considerably slower because Sr diffusivity in olivine (Chakraborty, 2010) is about 6 orders of magnitudes slower than in diopside (Sneeringer et al., 1984) and comparable to REE diffusion in olivine, orthopyroxene and clinopyroxene. Therefore, unless transient events of heating or fluid percolation occur, it is likely that isotope disequilibrium due to metasomatism can be preserved at the mantle xenolith scale for hundreds of Myr also at higher temperatures (up to 1100–1200 °C) than those recorded by the examined samples (i.e. 800–900 °C).

6. Conclusions

In this study we report large compositional and Sr isotope variations in grains of Ti-rich LIMA (LIndsleyite–MAthiasite group) from the ~84 Ma Bultfontein kimberlite (Kimberley, South Africa). Previous U–Pb dating constrained the formation of these LIMA minerals (plus clinopyroxene, phlogopite and minor Fe–Ni sulfides) in the lithospheric mantle (~100–120 km of depth) to be coeval with the ~180 Ma Karoo magmatic event (Giuliani et al., 2014b). SEM-BSE images show that in each xenolith up to four distinct LIMA types can coexist in the same grain. Major element and *in situ* Sr isotope measurements reveal that each LIMA type has a specific composition, distinct from the other LIMA groups. This requires that fluids with variable composition infiltrated the lithospheric mantle beneath Kimberley, broadly at the same time (i.e. within a few thousands to millions of years), and produced (or equilibrated with) the same LIMA-bearing metasomatic assemblage. We therefore attribute the isotopic variations exhibited by LIMA (and clinopyroxene) minerals to disequilibrium associated with mantle metasomatism; and speculate that the structure of LIMA, coupled with the moderate temperature (~800–900 °C) of the lithospheric mantle where these samples resided, favoured preservation of geochemical heterogeneities at the grain scale. A profound implication of this work is that hot fluids infiltrating a rock do not necessarily cause local equilibration at the cm scale as commonly assumed.

Simple modelling of solid-state diffusion at temperature (~1000–1200 °C) typical of the intermediate-deep lithospheric mantle shows that isotopic heterogeneities can be maintained for hundreds of Myr unless transient events of heating or fluid percolation occur. Radiogenic isotope disequilibrium associated with metasomatism may therefore be more common in mantle xenoliths than previously recognised. If so, measurements of large aliquots of separated minerals may yield mixed signatures and, hence, erroneous petrological interpretations. Consequently, this study provides strong evidence of the risks associated with undertaking isotopic work on mantle rocks equilibrated at $T < 1000$ °C, and perhaps up to 1200 °C, using bulk mineral analyses without prior assessment of compositional variations at the grain and sample scale. Further application of *in situ* micro-analytical techniques to mantle minerals coupled with measurements of multiple small aliquots of separated grains by solution methods should provide additional insights into the complexity of fluid processes in the Earth's interiors.

Acknowledgements

We would like to thank Graham Hutchinson for support with the EMP analyses at the University of Melbourne, and the De Beers Group for providing access to the studied samples. We acknowledge constructive reviews from Richard Hinton and Steve Haggerty, and efficient editorial handling of Frederic Moynier. AG acknowledges funding from the Australian Research Council through a DECRA award (DE-150100009). GRD received funding from the European Research Council under the European Union's Seventh Framework Programme (FP7/2007-2013; ERC grant agreement n. 319209). This is contribution 1030 from the ARC Centre of Excellence for Core to Crust Fluid Systems (www.ccfs.mq.edu.au) and 1189 from the GEMOC Key Centre (www.gemoc.mq.edu.au).

Appendix A. Supplementary material

Supplementary material related to this article can be found online at https://doi.org/10.1016/j.epsl.2017.11.014.

References

Aulbach, S., Griffin, W.L., Pearson, N.J., O'Reilly, S.Y., 2013. Nature and timing of metasomatism in the stratified mantle lithosphere beneath the central Slave craton (Canada). Chem. Geol. 352, 153–169.

Carlson, R.W., Irving, A.J., 1994. Depletion and enrichment history of subcontinental lithospheric mantle: an Os, Sr, Nd and Pb isotopic study of ultramafic xenoliths from the northwestern Wyoming Craton. Earth Planet. Sci. Lett. 126, 457–472.

Chakraborty, S., 2010. Diffusion coefficients in olivine, wadsleyite and ringwoodite. Rev. Mineral. Geochem. 72, 603–639.

Cherniak, D.J., Liang, Y., 2007. Rare earth element diffusion in natural enstatite. Geochim. Cosmochim. Acta 71, 1324–1340.

Dawson, J.B., Hill, P., Kinny, P., 2001. Mineral chemistry of a zircon-bearing, composite, veined and metasomatised upper-mantle peridotite xenolith from kimberlite. Contrib. Mineral. Petrol. 140, 720–733.

Erlank, A.J., Waters, F.G., Hawkesworth, C.J., Haggerty, S.E., Allsopp, H.L., Rickard, R.S., Menzies, M., 1987. Evidence for mantle metasomatism in peridotite nodules from the Kimberley Pipes, South Africa. In: Menzies, M.A., Hawkesworth, C.J. (Eds.), Mantle Metasomatism. Academic Press, London, pp. 221–311.

Giuliani, A., Fiorentini, M.L., Martin, L.A.J., Farquhar, J., Phillips, D., Griffin, W.L., LaFlamme, C., 2016a. Sulfur isotope composition of metasomatised mantle xenoliths from the Bultfontein kimberlite (Kimberley, South Africa): contribution from subducted sediments and the effect of sulfide alteration on S isotope systematics. Earth Planet. Sci. Lett. 445, 114–124.

Giuliani, A., Kamenetsky, V.S., Kendrick, M.A., Phillips, D., Goemann, K., 2013a. Nickel-rich metasomatism of the lithospheric mantle by pre-kimberlitic alkali-S–Cl-rich C–O–H fluids. Contrib. Mineral. Petrol. 165, 155–171.

Giuliani, A., Phillips, D., Fiorentini, M.L., Kendrick, M.A., Maas, R., Wing, B.A., Woodhead, J.D., Bui, T.H., Kamenetsky, V.S., 2013b. Mantle oddities: a sulphate fluid preserved in a MARID xenolith from the Bultfontein kimberlite (Kimberley, South Africa). Earth Planet. Sci. Lett. 376, 74–86.

Giuliani, A., Phillips, D., Kamenetsky, V.S., Goemann, K., 2016b. Constraints on kimberlite ascent mechanisms revealed by phlogopite compositions in kimberlites and mantle xenoliths. Lithos 240–243, 189–201.

Giuliani, A., Phillips, D., Kamenetsky, V.S., Kendrick, M.A., Wyatt, B.A., Goemann, K., Hutchinson, G., 2014a. Petrogenesis of mantle polymict breccias: insights into mantle processes coeval with kimberlite magmatism. J. Petrol. 55, 831–858.

Giuliani, A., Phillips, D., Maas, R., Woodhead, J.D., Kendrick, M.A., Greig, A., Armstrong, R.A., Chew, D., Kamenetsky, V.S., Fiorentini, M.L., 2014b. LIMA U–Pb ages link lithospheric mantle metasomatism to Karoo magmatism beneath the Kimberley region, South Africa. Earth Planet. Sci. Lett. 401, 132–147.

Giuliani, A., Phillips, D., Woodhead, J.D., Kamenetsky, V.S., Fiorentini, M.L., Maas, R., Soltys, A., Armstrong, R.A., 2015. Did diamond-bearing orangeites originate from MARID-veined peridotites in the lithospheric mantle? Nat. Commun. 6, 6837.

Giuliani, A., Soltys, A., Phillips, D., Kamenetsky, V.S., Maas, R., Goemann, K., Woodhead, J.D., Drysdale, R.N., Griffin, W.L., 2017. The final stages of kimberlite petrogenesis: petrography, mineral chemistry, melt inclusions and Sr–C–O isotope geochemistry of the Bultfontein kimberlite (Kimberley, South Africa). Chem. Geol. 455, 342–356.

Griffin, W.L., Pearson, N.J., Andersen, T., Jackson, S.E., O'Reilly, S.Y., Zhang, M., 2014. Sources of cratonic metasomatic fluids: in situ LA-MC-ICPMS analysis of Sr, Nd, Hf and Pb isotopes in Lima from the Jagersfontein Kimberlite. Am. J. Sci. 314, 435–461.

Gunther, M., Jagoutz, E., 1994. Isotopic disequilibria (Sm/Nd, Rb/Sr) between minerals of coarse grained, low temperature garnet peridotites from Kimberley Floors, Southern Africa. In: Meyer, H.O.A., Leonardos, O.H. (Eds.), Kimberlites, Related Rocks and Mantle Xenoliths. 5th International Kimberlite Conference, Araxa, Brazil. In: CPRM Special Publication, pp. 354–365.

Haggerty, S.E., Smyth, J.R., Erlank, A.J., Rickard, R.S., Danchin, R.V., 1983. Lindsleyite (Ba) and mathiasite (K): two new chromium-titanates in the crichtonite series from the upper mantle. Am. Mineral. 68, 494–505.

Hamilton, M.A., Pearson, D.G., Stern, R.A., Boyd, F.R., 1998. Constraints on MARID petrogenesis: SHRIMP II U–Pb zircon evidence for pre-eruption metasomatism at Kampfersdam. In: Gurney, J.J., Gurney, J.L., Pascoe, M.D., Richardson, S.H. (Eds.), 7th International Kimberlite Conference, Extended Abstracts. Red Roof Design, Capetown, pp. 296–298.

Hawkesworth, C.J., Erlank, A.J., Kempton, P.D., Waters, F.G., 1990. Mantle metasomatism: isotope and trace-element trends in xenoliths from Kimberley, South Africa. Chem. Geol. 85, 19–34.

Ionov, D.A., Mukasa, S.B., Bodinier, J.-L., 2002. Sr–Nd–Pb isotopic compositions of peridotite xenoliths from Spitsbergen: numerical modelling indicates Sr–Nd decoupling in the mantle by melt percolation metasomatism. J. Petrol. 43, 2261–2278.

Jagoutz, E., Carlson, R.W., Lugmair, G.W., 1980. Equilibrated Nd-unequilibrated Sr isotopes in mantle xenoliths. Nature 286, 708–710.

Kinny, P.D., Dawson, J.B., 1992. A mantle metasomatic injection event linked to late Cretaceous kimberlite magmatism. Nature 360, 726–728.

Klein-BenDavid, O., Pearson, D.G., Nowell, G.M., Ottley, C., McNeill, J.C.R., Cartigny, P., 2010. Mixed fluid sources involved in diamond growth constrained by Sr–Nd–Pb–C–N isotopes and trace elements. Earth Planet. Sci. Lett. 289, 123–133.

Konzett, J., Armstrong, R.A., Sweeney, R.J., Compston, W., 1998. The timing of MARID metasomatism in the Kaapvaal mantle: an ion probe study of zircons from MARID xenoliths. Earth Planet. Sci. Lett. 160, 133–145.

Konzett, J., Wirth, R., Hauzenberger, C., Whitehouse, M., 2013. Two episodes of fluid migration in the Kaapvaal Craton lithospheric mantle associated with Cretaceous kimberlite activity: evidence from a harzburgite containing a unique assemblage of metasomatic zirconium-phases. Lithos 182–183, 165–184.

Konzett, J., Yang, H., Frost, D.J., 2005. Phase relations and stability of magnetoplumbite- and crichtonite-series phases under upper-mantle P–T conditions: an experimental study to 15 GPa with implications for LILE metasomatism in the lithospheric mantle. J. Petrol. 46, 749–781.

Koornneef, J.M., Davies, G.R., Dopp, S.P., Vukmanovic, Z., Nikogosian, I.K., Mason, P.R.D., 2009. Nature and timing of multiple metasomatic events in the subcratonic lithosphere beneath Labait, Tanzania. Lithos 112S, 896–912.

Kramers, J.D., Roddick, J.C.M., Dawson, J.B., 1983. Trace element and isotope studies on veined, metasomatic and "MARID" xenoliths from Bultfontein, South Africa. Earth Planet. Sci. Lett. 65, 90–106.

Liati, A., Franz, L., Gebauer, D., Fanning, C.M., 2004. The timing of mantle and crustal events in South Namibia, as defined by SHRIMP-dating of zircon domains from a garnet peridotite xenolith of the Gibeon Kimberlite Province. J. Afr. Earth Sci. 39, 147–157.

McDonough, W.F., McCulloch, M.T., 1987. The southeast Australian lithospheric mantle: isotopic and geochemical constraints on its growth and evolution. Earth Planet. Sci. Lett. 86, 327–340.

O'Reilly, S., Griffin, W.L., 2013. Mantle metasomatism. In: Metasomatism and the Chemical Transformation of Rock. Springer, Berlin, Heidelberg, pp. 471–533.

Paton, C., Woodhead, J.D., Hergt, J.M., Phillips, D., Shee, S., 2007. Strontium isotope analysis of kimberlitic groundmass perovskite via LA-MC-ICP-MS. Geostand. Geoanal. Res. 31, 321–330.

Pearson, D.G., Canil, D., Shirey, S.B., 2003. Mantle samples included in volcanic rocks: xenoliths and diamonds. In: Carlson, R. (Ed.), Treatise on Geochemistry, vol. 2, The Mantle and Core. Pergamon, Oxford, pp. 171–275.

Pearson, D.G., Shirey, S.B., Carlson, R.W., Boyd, F.R., Pokhilenko, N.P., Shimizu, N., 1995. Re–Os, Sm–Nd, and Rb–Sr isotope evidence for thick Archaean lithospheric mantle beneath the Siberian craton modified by multistage metasomatism. Geochim. Cosmochim. Acta 59, 959–977.

Pin, C., Briot, D., Bassin, C., Poitrasson, F., 1994. Concomitant separation of strontium and samarium-neodymium for isotopic analysis in silicate samples, based on specific extraction chromatography. Anal. Chim. Acta 298, 209–217.

Raczek, I., Jochum, K.P., Hofmann, A.W., 2003. Neodymium and strontium isotope data for USGS reference materials BCR-1, BCR-2, BHVO-1, BHVO-2, AGV-1, AGV-2, GSP-1, GSP-2 and eight MPI-DING reference glasses. Geostand. Newsl. 27, 173–179.

Richardson, S.H., Erlank, A.J., Hart, S.R., 1985. Kimberlite-borne garnet peridotite xenoliths from old enriched subcontinental lithosphere. Earth Planet. Sci. Lett. 75, 116–128.

Schmidberger, S.S., Simonetti, A., Francis, D., 2003. Small-scale Sr isotope investigation of clinopyroxenes from peridotite xenoliths by laser ablation MC-ICP-MS: implications for mantle metasomatism. Chem. Geol. 199, 317–329.

Shu, Q., Brey, G.P., Gerdes, A., Hoefer, H.E., 2014. Mantle eclogites and garnet pyroxenites – the meaning of two-point isochrons, Sm–Nd and Lu–Hf closure temperatures and the cooling of the subcratonic mantle. Earth Planet. Sci. Lett. 389, 143–154.

Shu, Q., Brey, G.P., Gerdes, A., Hofer, H.E., 2013. Geochronological and geochemical constraints on the formation and evolution of the mantle underneath the Kaapvaal craton: Lu–Hf and Sm–Nd systematics of subcalcic garnets from highly depleted peridotites. Geochim. Cosmochim. Acta 113, 1–20.

Simon, N.S.C., Carlson, R.W., Pearson, D.G., Davies, G.R., 2007. The origin and evolution of the Kaapvaal Cratonic lithospheric mantle. J. Petrol. 48, 589–625.

Sneeringer, M., Hart, S.R., Shimizu, N., 1984. Strontium and samarium diffusion in diopside. Geochim. Cosmochim. Acta 48, 1589–1608.

Sobolev, N.V., Kaminsky, F.V., Griffin, W.L., Yefimova, E.S., Win, T.T., Ryan, C.G., Botkunov, A.I., 1997. Mineral inclusions in diamonds from the Sputnik kimberlite pipe, Yakutia. Lithos 39, 135–157.

Soltys, A., Giuliani, A., Phillips, D., Kamenetsky, V.S., Maas, R., Woodhead, J., Rodemann, T., 2016. In-situ assimilation of mantle minerals by kimberlitic magmas — direct evidence from a garnet wehrlite xenolith entrained in the Bultfontein kimberlite (Kimberley, South Africa). Lithos 256–257, 182–196.

Tappe, S., Simonetti, A., 2012. Combined U–Pb geochronology and Sr–Nd isotope analysis of the Ice River perovskite standard, with implications for kimberlite and alkaline rock petrogenesis. Chem. Geol. 304–305, 10–17.

Van Orman, J., Grove, T., Shimizu, N., Layne, G., 2002. Rare earth element diffusion in a natural pyrope single crystal at 2.8 GPa. Contrib. Mineral. Petrol. 142, 416–424.

Van Orman, J.A., Grove, T.L., Shimizu, N., 2001. Rare earth element diffusion in diopside: influence of temperature, pressure, and ionic radius, and an elastic model for diffusion in silicates. Contrib. Mineral. Petrol. 141, 687–703.

Villa, I.M., De Bièvre, P., Holden, N.E., Renne, P.R., 2015. IUPAC-IUGS recommendation on the half life of ^{87}Rb. Geochim. Cosmochim. Acta 164, 382–385.

Walker, R.J., Carlson, R.W., Shirey, S.B., Boyd, F.R., 1989. Os, Sr, Nd, and Pb isotope systematics of southern African peridotite xenoliths: implications for the chemical evolution of subcontinental mantle. Geochim. Cosmochim. Acta 53, 1583–1595.

Woodhead, J., Hergt, J., Giuliani, A., Phillips, D., Maas, R., 2017. Tracking continental-scale modification of the Earth's mantle using zircon megacrysts. Geochem. Perspect. Lett. 4, 1–6.

Woodhead, J., Hergt, J., Phillips, D., Paton, C., 2009. African kimberlites revisited: in situ Sr-isotope analysis of groundmass perovskite. Lithos 112S, 311–317.

Woodhead, J., Swearer, S., Hergt, J., Maas, R., 2005. In situ Sr-isotope analysis of carbonates by LA-MC-ICP-MS: interference corrections, high spatial resolution and an example from otolith studies. J. Anal. At. Spectrom. 20, 22–27.